ADVANCED MATERIALS INTERFACES
www.advmatinterfaces.de

Engineered Creation of Periodic Giant, Nonuniform Strains in MoS_2 Monolayers

Elena Blundo, Cinzia Di Giorgio, Giorgio Pettinari, Tanju Yildirim, Marco Felici, Yuerui Lu, Fabrizio Bobba, and Antonio Polimeni**

The realization of ordered strain fields in 2D crystals is an intriguing perspective in many respects, including the instauration of novel transport regimes and enhanced device performances. However, the current straining techniques hardly allow to reach strains higher than ≈3% and in most cases there is no control over the strain distribution. In this work, a method is demonstrated to subject micrometric regions of atomically thin molybdenum disulfide (MoS_2) to giant strains with the desired ordering. Selective hydrogen-irradiation of bulk flakes allows the creation of arrays of size/position-controlled monolayer domes containing pressurized hydrogen. However, the gas pressure is ruled by energy minimization, limiting the extent and geometry of the mechanical deformation of the 2D membrane. Here, a protocol is developed to create a mechanical constraint, that alters remarkably the morphology of the domes, otherwise subject to universal scaling laws, as demonstrated by atomic force microscopy. This enables the realization of unprecedented periodic configurations of large strain gradients—estimated by numerical simulations—with the highest strains being close to the rupture critical values (>10%). The creation of such high strains is confirmed by Raman experiments. The method proposed here represents an important step toward the strain engineering of 2D crystals.

In a solid-state environment, the possibility to engender novel fundamental effects or to achieve favorable conditions for the realization of devices typically relies on the ability to modify the basic properties of crystalline materials. The creation of alloys and heterostructures, the introduction of dopants, and strain are common tools. Among them, strain is particularly relevant for 2D crystals—such as graphene and transition metal dichalcogenides (TMDs)—where flexibility and robustness[1,2] couple to a high sensitivity to mechanical deformations.[3] For TMDs, which are direct gap semiconductors[4–6] characterized by a strong spin–orbit coupling[7] in the monolayer (ML) limit, tensile strain leads to a sizeable reduction and modification of the band gap,[8–12] up to turning it from direct to indirect.[13–16] Extremely high strains (≳10%)[2] can be applied reversibly, and absorption, emission, and carriers' mobility and lifetime can thus be modulated[10,13,17,18] on-demand. Therefore, the application of strain-engineering protocols to TMDs holds a great potentiality for optoelectronics, spin-, and valley-tronics. Several methods for straining atomically thin materials have been developed, including bending apparatuses,[11,19] deposition on pillars[20] or nanocones,[21] epitaxial growth of superlattices[22] or growth on curved structures[23] and creation of bulges by means of specific devices,[10,24] or spontaneous formation of domes.[25–27] Most of these methods, however, enable only a modest strain transfer to the 2D membrane (≈1–2%). Bulges or domes exploit the pressure exerted on the crystal by trapped gases and nowadays represent the most efficient method for achieving strained 2D membranes, also allowing a certain degree of control over the spatial distribution of the deformation.[10,26] This is particularly relevant for ML-TMDs, where the creation of strain gradients leads to a seamless reduction of

E. Blundo, Prof. M. Felici, Prof. A. Polimeni
Physics Department
Sapienza University of Rome
Rome 00185, Italy
E-mail: elena.blundo@uniroma1.it; antonio.polimeni@roma1.infn.it

Dr. C. Di Giorgio, Prof. F. Bobba
Department of Physics E.R: Caianiello
University of Salerno
Fisciano 84084, Italy

Dr. C. Di Giorgio, Prof. F. Bobba
SuPerconducting and other INnovative Materials and Devices Institute
National Research Council
Fisciano 84084, Italy

Dr. G. Pettinari
Institute for Photonics and Nanotechnologies
National Research Council
Rome 00156, Italy

Dr. T. Yildirim
Center for Functional Sensor & Actuator (CFSN)
National Institute for Materials Science (NIMS)
Tsukuba, Ibaraki 305-0044, Japan

Dr. T. Yildirim, Prof. Y. Lu
Research School of Electrical, Energy and Materials Engineering
College of Engineering and Computer Science
The Australian National University
Canberra ACT2601, Australia

The ORCID identification number(s) for the author(s) of this article can be found under https://doi.org/10.1002/admi.202000621.

DOI: 10.1002/admi.202000621

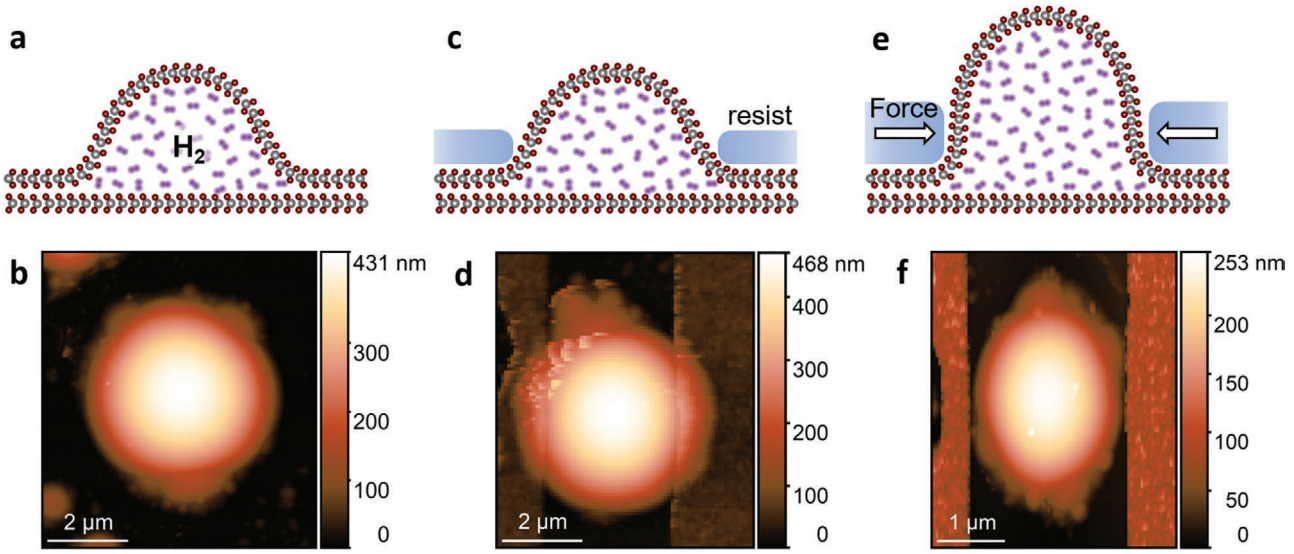

Figure 1. Creation of domes without and with a constraint. a) Sketch of a MoS_2 dome formed via hydrogen-irradiation of a bulk flake. The dome is one layer thick and cages molecular hydrogen. b) AFM image of a dome created with the process schematized in panel (a). The footprint radius of the dome and its maximum height are $R = 2.57$ μm and $h_m = 422$ nm, respectively. Hence $h_m/R = 0.164$. c) Sketch of a MoS_2 dome formed within a mask and totally filling the opening. The resist represents a spatial boundary, without altering the dome natural shape, which is thus analogous to that of panel (a). (d) AFM image of a dome within a corridor (width equal to 3.06 μm) in a patterned sample with a 40 nm thick mask, showing how the dome is able to raise the resist. The dome thus maintains its circular shape, with $R = 2.64$ μm and $h_m = 453$ nm, resulting in $h_m/R = 0.171$. e) Sketch of a dome in the case of a resist that represents a strong constraint, limiting the dome expansion and thus leading to an increased pressurization of the inner gas and to an increased aspect ratio. f) AFM image of a dome within a corridor (width equal to 2.25 μm) in a patterned sample with an 80 nm thick mask, showing how in this case the dome is elliptically deformed due to the constraint imposed by the resist, as schematized in panel (e). The radius of the dome measured in the direction perpendicular to the corridor is $R = 1.11$ μm, while the height of the dome is $h_m = 245$ nm. Hence, in this case a higher aspect ratio $h_m/R = 0.221$ is achieved due to the effect of the thick resist.

the band gap[13,26] and can result in pseudo-gauge fields able to rule the quasi-particles' motion.[28] In turn, stable and periodic strain modulations are promising for broadband light absorption and carriers' harvesting,[13,18] and for the generation of persistent currents,[29] which make them on the one side apt to photovoltaics, photocatalysis, and photodetection devices,[18] and, on the other side, a fruitful platform for the observation of novel physical phenomena. Furthermore, strain represents an effective tool for enhancing the electrochemical activity of TMDs.[21,30,31] However, the great promise of these systems is hindered by the fact that the durability of the bulges is limited to few weeks,[10,24] while the deformation of the domes is governed by energy minimization,[25,32,33] that establishes an upper bound for the achievable strains. Here, we move a step further by developing a method to achieve unprecedented periodic, durable, and extremely high strain gradients in MoS_2 through the engineered creation of domes.

In this paper, bulk flakes are mechanically exfoliated on SiO_2/Si substrates and hydrogen-irradiated—as described in ref. [26], where H ions have been shown to penetrate through the basal plane of the irradiated crystal, leading to the formation and coalescence of molecular hydrogen (H_2). This results in the creation of nano-/micrometric isolated spherical domes or conglomerates of domes—with a thickness of just one S-Mo-S layer and sealing the trapped H_2 gas—on the flake surface,[26] as shown in **Figure 1**a,b. In order to achieve control over the size and position of the domes, several samples were prepared by depositing a hydrogen silesquioxane (HSQ) negative-tone e-beam resists—with thickness in between 20 and 50 nm—on MoS_2 bulk flakes prior to irradiation (see the Experimental Section). Octagonal openings with different sizes were then created in the polymeric masks via electron-beam lithography (EBL), as detailed in Note S1 in the Supporting Information. The samples were then H-irradiated, allowing the formation of the domes only within the openings or in the corridors between the HSQ-covered regions of the flake. This patterning procedure was proposed in a previous work (ref. [26]) for WS_2, representing a tool for a selective proton incorporation and localized hydrogen formation. The domes created in that work had however dimensions smaller than the opening size. To increase the sample homogeneity and narrow the size distribution, we here optimized the irradiation procedure, as discussed in Note S1 in the Supporting Information: This allowed us to form domes that are filling the openings, as schematized in Figure 1c. The morphological properties of the domes were probed by atomic force microscopy (AFM, see the Experimental Section). As theoretically predicted[25,32,33] and experimentally demonstrated,[25–27] atomically thin domes feature a universal aspect ratio (h_m/R, with h_m maximum height and R footprint radius) which remains constant independently of the radius value. For MoS_2 domes on MoS_2 flakes, the universal h_m/R value is 0.16,[25,26] that sets the limit to the maximum achievable strain to ≈3.7% (as discussed later). We find the same average h_m/R value for random domes as well as for patterned domes created with the procedure discussed so far, even when filling the openings. Thus, the presence of the resist does not alter the mechanics of the formation process, while just representing a spatial boundary. However, if one were able to realize

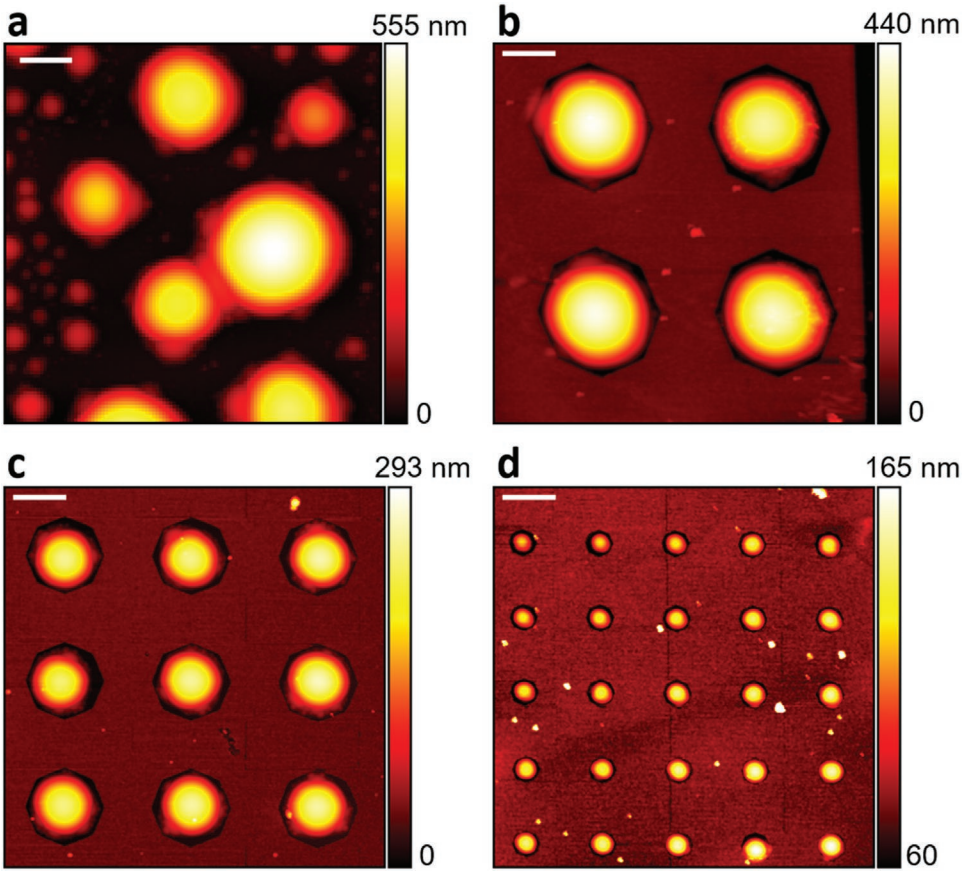

Figure 2. Formation of random and patterned arrays of MoS_2 domes. a) AFM image of a 15 × 15 μm² area of a proton-irradiated MoS_2 flake. Many domes with different dimensions (the largest dome has a footprint diameter $D = 6.03$ μm) formed on the flake surface following the irradiation process. The aspect ratio for these domes varies between about 0.14 and 0.18. b–d) Same for MoS_2 flakes patterned with an 80 nm thick mask with openings of size b) $S = 5$ μm, c) 3 μm, and d) 1 μm. The diameter of the domes is in this case determined by the size of the opening, and higher aspect ratios with respect to the random domes are obtained, as discussed in the following. The scale bars correspond to 2 μm, while the origin of the *z*-axis is set at the flake surface.

a boundary acting as a strong constraint, the force exerted by such constraint should lead to an increased pressurization of the inner gas and the lateral expansion of the dome during the formation process would be halted. As a combined effect of these two factors, the dome would expand vertically and a higher deformation of the 2D membrane would be achieved, thus leading to an increase of the internal energy of the trapped gas.[34] Since the mechanical behavior of 2D blisters is governed by the total energy minimization, the increased contribution of the gas internal energy should be balanced by the elastic contribution, and hence the in-plane strain would increase.[34] This picture is supported by preliminary numerical simulations discussed in Note S2 in the Supporting Information. The recipe discussed so far has proven inefficacious to achieve such a goal, since whenever high pressurization is attained, the domes are able to raise the resist, as shown in Figure 1d. We thus modified the patterning procedure, with the aim of achieving a stronger boundary, as in Figure 1e. To do that, we patterned several samples via realizing resists with different thicknesses, in between 20 and 100 nm, which were achieved by varying the resist concentration and spinning speed. The actual thickness of the mask was systematically measured by AFM, as described in Note S2 in the Supporting Information. Since high temperatures (>100 °C) are known to cause a hardening of the resist (that could make it more effective in acting as a constraint), the samples were heated for ≈1 h before H irradiation. The effects of an increased resist thickness are immediately apparent by looking at Figure 1f, where a dome is compressed due to the presence of an 80 nm thick mask nearby. Thus, we exploited this procedure to realize ordered arrays of MoS_2 domes with different sizes during the same irradiation process—as shown in **Figure 2** for a mask with openings of size $S = 5$, 3, and 1 μm—and performed second harmonic generation measurements to verify that the patterned domes are just one layer thick[35,36] (see Figure S1, Supporting Information). AFM measurements allow to address the effect of the constraint quantitatively, as discussed in **Figure 3**: The dome in Figure 3a is a typical random one with $h_m/R = 0.165$, while the patterned domes in panels (b)–(d) were created in a pattern with thickness $t \sim 50$–60 nm and have $h_m/R = 0.186$ ($S = 5$ μm, Figure 3b), 0.219 ($S = 3$ μm, Figure 3c), 0.264 ($S = 1$ μm, Figure 3d). Clearly, in this case, the mask acts as a strong constraint over the spontaneous formation of the domes (see also Note S2, Supporting Information) allowing to overcome the natural, universal limit of the aspect

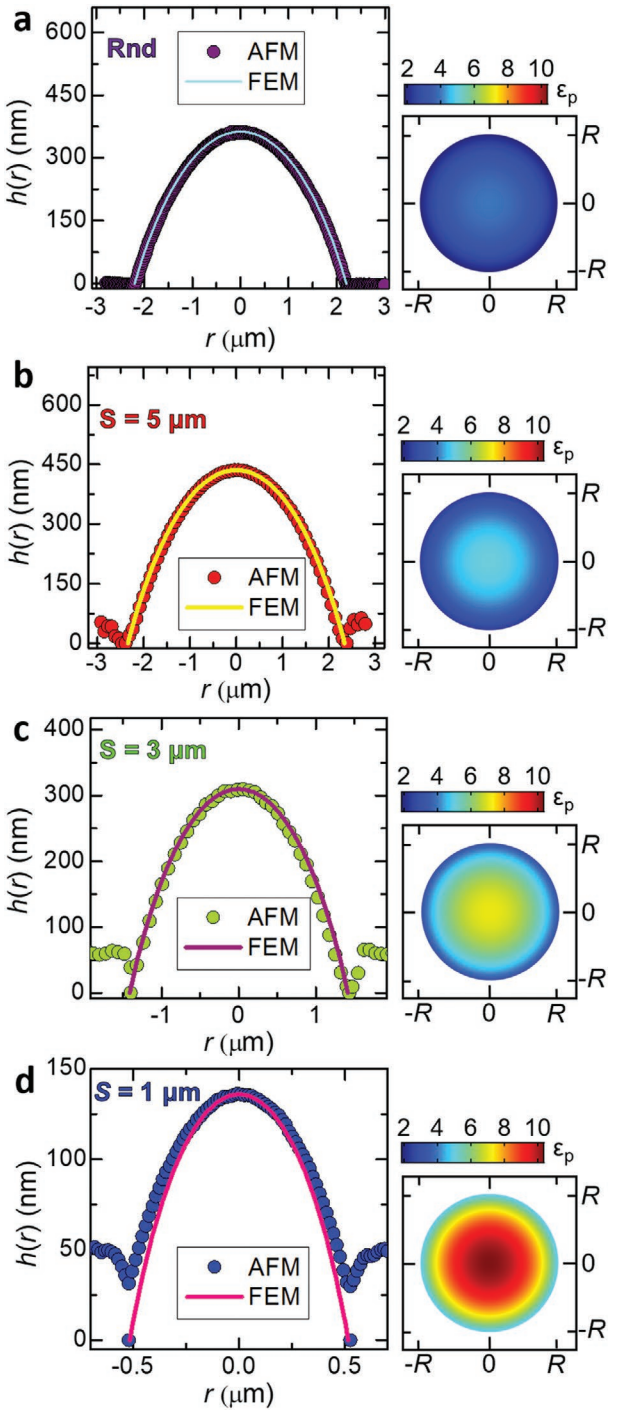

Figure 3. Height profile and total in-plane strain in MoS_2 domes. a–d) Left panels: AFM height profiles (colored dots) versus the distance from the center (r) along a diameter of a random (a), and three patterned domes created in openings with size b) $S = 5$ μm, c) $S = 3$ μm, and d) $S = 1$ μm. For the dome in panel (d), the AFM tip was not able to measure its base and the two points at 0 were set by measuring the thickness of the resist in a nearby corridor. The ratio between the vertical and horizontal axis is the same for the four plots, to emphasize the differences in the aspect ratios of the domes. The solid lines represent the profiles calculated via FEM simulations. Right panels: spatial distribution of the total percentage in-plane strain for the domes on the left, according to the color bar displayed on top. The same scale has been used for the four plots.

ratio. This is particularly relevant because the establishment of a protocol to exceed the universal limit paves the way for achieving unprecedented strains. To quantify the strain values, we notice that i) atomically thin domes are characterized by an anisotropic tensile in-plane strain that increases from the edge toward the summit,[13,26,37] where it becomes isotropic biaxial; ii) due to the analogous effect of the different in-plane strain components (i.e., the radial, ε_r, and circumferential, ε_t, components for the domes, due to the spherical symmetry of their shape[26]) on the electronic properties of TMDs,[8] one can quantify the strain acting on the 2D membrane by translating the anisotropic strain tensor into a total in-plane strain defined as[13] $\varepsilon_p = \varepsilon_r + \varepsilon_t$.

According to Hencky's model,[10,38] MoS_2 domes are characterized at the summit by a total in-plane strain[26] $\varepsilon_p^{summit} = 2 \cdot f(\nu) \cdot (h_m/R)^2$, with $f(\nu) = 0.721$, while numerical methods have to be employed to calculate the strain field distribution across the domes' surface. Finite-element method (FEM) calculations[26] were thus used to simulate the profiles of the domes (that are in good agreement with the AFM profiles, see Figure 3) and calculate the strain components.[13,26] In the right panels of Figure 3a–d, we show the spatial distribution of ε_p associated with the domes on the left. The same color-scale has been used for all the plots in order to emphasize the remarkable increase of the strain values for increased aspect ratios. Such increase is a direct consequence of the augmented H_2 pressure, estimated via FEM calculations to go from 7.7 atm (panel a), to 11 atm (b), to 29 atm (c) to 136 atm (d). Calculations concerning the geometry and degree of isotropy of the strain tensor and its effect on the exciton transitions are discussed in Note S3 in the Supporting Information. Indeed, extremely high strains—larger than 10%—are achieved for domes created in small openings ($S = 1$ μm). To our knowledge, such high strains—close to the rupture limit—can only be achieved by indentation of suspended monolayers[2] or with bulging devices,[10] but in the former case the membrane cannot stand alone, while in the latter case the structures are not durable.[10,24] With our method, instead, the domes typically last for years[26] (part of the measurements performed on a sample in this work was taken 2 years after creating the domes) and can be easily integrated in experimental apparatuses or devices.

The general validity of this result is confirmed by the AFM statistical analysis of the aspect ratios shown in **Figure 4**a, performed on several different samples patterned with masks of thickness t between 50 and 100 nm. The aspect ratios range—on average—from 0.191 ± 0.015 for domes in openings with $S = 5$ μm, to 0.216 ± 0.018 for $S = 3$ μm, to 0.274 ± 0.026 for $S = 1$ μm, while in random domes we get 0.159 ± 0.018. The average ratio in patterned domes decreases to ≈0.18 (almost independently of S) for $t \sim 37$ nm, to approach the universal value for $t \sim 25$ nm (see Figure 4b). To highlight the role played by the mask in altering the aspect ratio, we used an AFM tip to apply an extra mechanical stress to a patterned dome ($S = 3$ μm) with $h_m/R = 0.206$ (Figure 4c, left). By pushing down the tip as described in Figure S2 in the Supporting Information, we induced a deflating process and separated the original dome in four smaller domes (Figure 4c, center), all with $h_m/R \sim 0.16$. Finally, by scanning the tip over the domes we induced them to coalesce, resulting in the formation of a single dome (Figure 4c,

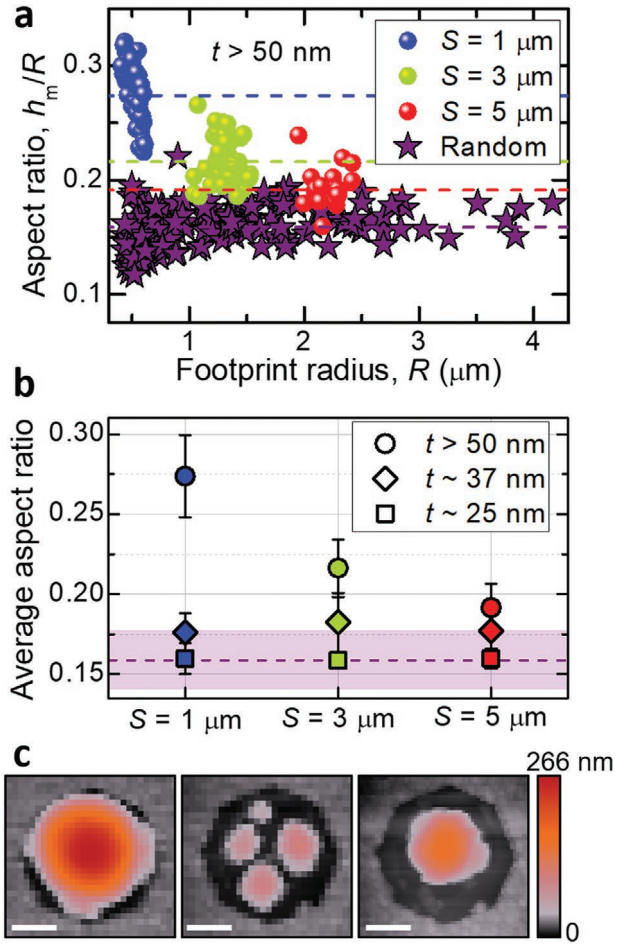

Figure 4. Increasing the aspect ratios and strains of the domes. a) Aspect ratios measured by AFM in patterned MoS_2 domes (openings with size $S = 1$ μm, blue dots; $S = 3$ μm, green dots; and $S = 5$ μm, red dots; resists with thickness 50 nm < t < 100 nm), and on random MoS_2 domes (purple stars) as a function of the footprint radius. The colored dashed lines highlight the average aspect ratios calculated for each set of data. b) Average aspect ratio calculated by the data in panel (a) (circles) and in samples with thinner resists ($t = 37 \pm 6$, rhombi; $t = 25 \pm 5$, squares) for different sizes of the openings. The purple dashed line highlights the average aspect ratio measured for random domes, and the shaded area provides the associated uncertainty. c) Left: AFM image of a patterned dome ($S = 3$ μm) with $h_m/R = 0.206$. Center: AFM image acquired after indentation of the dome with the AFM tip. The dome was caused to deflate giving rise to four smaller domes with aspect ratio of about 0.16. Right: The four domes were induced to coalesce by the AFM tip, resulting in a single dome with $h_m/R = 0.169$. The whole process took ≈10 min. The white scale bar is 1 μm. The z range varies accordingly to the color bar.

right). This dome has smaller dimensions than the original one due to the initial deflation, and $h_m/R = 0.169$ (see Figure S2, Supporting Information), which is very close to the universal ratio.

The high strains here achieved should result in significant shifts of the Raman modes[10,11,26,39,40] and exciton energies.[8–11,13,17,18,26] Therefore, micro-Raman (μ-Raman) measurements (see the Experimental Section) were performed on domes patterned in thick resists, like those in **Figure 5**a. In Figure 5b, we show the average total in-plane strain at the summit of such domes (ε_p^{summit}, calculated via Hencky's model or, equivalently, by FEM calculations). While the structures created in openings with $S = 1$ μm have the largest aspect ratio, the spatial resolution of our optical setup (see the Experimental Section) is not enough to perform spatially resolved optical measurements, as clear from Figure 5a, where the white scale bar corresponds to the size of the laser-spot. For this reason, domes in openings with $S = 3$ μm—with ε_p^{summit} on average equal to (6.7 ± 1.1)%—were chosen, as the best trade-off between high ratios and acceptable spatial resolution.

In Figure 5c, we show a comparison between the μ-Raman spectrum acquired on top of a random dome (purple) and of a patterned dome (green), in the region of the in-plane E^1_{2g} and out-of-plane A_{1g} modes (see the inset). The chosen random dome has diameter similar to the patterned dome. For each mode, the peaks at higher frequency—highlighted by dashed gray lines—originate from the bulk flake beneath the domes, while the lower-frequency peaks originate from the domes. Notably, Figure 5c points to a significant redshift of both the Raman modes in the patterned dome. To verify the consistency of our results with the measured aspect ratios, in Figure 5d we plot the Raman red-shifts for the E^1_{2g} mode (with respect to a strain-free ML) versus ε_p^{summit}, measured for several patterned ($S = 3$ μm) and random domes with similar dimensions. As expected, the tensile biaxial strain induces a softening of the modes that varies linearly with strain, with a red-shift rate of (2.2 ± 0.1) cm^{-1} $\%^{-1}$ and a Grüneisen parameter[41] $\gamma_{E^1_{2g}} = 0.58 \pm 0.03$. This result agrees well with previous estimations of $\gamma_{E^1_{2g}} = 0.6$ in ref. [39], 0.65 in ref. [40], and 0.68 in ref. [8], thus providing further confirmation of the enormous strains achieved with our method. The behavior of the A_{1g} mode, which is more subjected to strain-induced intensity modulations, is discussed in Note S4 in the Supporting Information. Finally, we also performed comparative micro-photoluminescence measurements on the domes, which also evidence a much larger strain in patterned domes, as shown in Figure S3 in the Supporting Information.

In conclusion, we have demonstrated a method to create periodic configurations of giant, nonuniform strains in MoS_2. This result can be achieved by engineering the process leading to the formation of one layer thick domes in proton-irradiated bulk flakes, via deposition of polymeric masks and EBL patterning. Such a strategy allows, in the first instance, to gain control over the position and size of the domes, and can be brought to a further level of thoroughness ensuing the ability to optimize the patterning procedure. In particular, we have here established the conditions to mechanically constrain the domes and enhance their aspect ratio remarkably. With this strategy, the internal pressure of the gas can be increased up to one order of magnitude, and natural built-in strain of the domes can be enhanced in excess of a factor of 3, thus creating periodic unprecedented strain gradients in the MoS_2 membrane over micrometric regions. In light of the high strains achieved, this system might represent a unique platform for the observation of novel phenomena, enabling the characterization of the optoelectronic, valley-, and spin-tronic fundamental properties of the k-space direct and indirect excitons in MoS_2 membranes under strongly anisotropic or

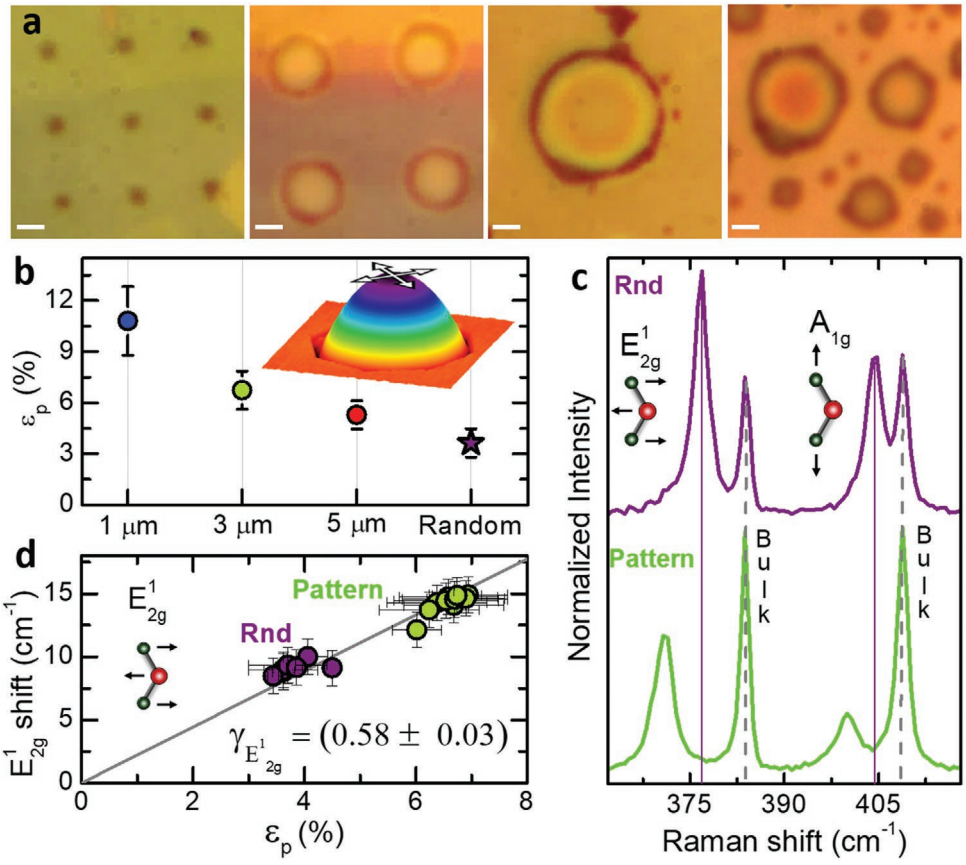

Figure 5. Micro-Raman measurements at the summit of random and patterned domes. a) Optical images acquired with a 100× objective with NA = 0.9 of (from left to right) patterned domes for $S = 1$ μm, for $S = 3$ μm, for $S = 5$ μm, and of random domes. The white scale bar is equal to 1.15 μm that approximately corresponds to the size of our laser spot. b) Average in-plane strain, ε_p, at the summit of patterned ($t > 50$ nm) and random domes, where strain is isotropic biaxial and reaches its maximum value. ε_p is given by the sum of the two equivalent radial and circumferential components ($\varepsilon_r = \varepsilon_t$) by Hencky's model, starting from the average values found for the aspect ratios in Figure 4a. Inset: AFM 3D image of a patterned dome depicting the two in-plane strain components (white arrows) at the dome summit. c) Raman spectra acquired at the summit of a patterned ($S = 3$ μm) dome (bottom, green) and of a random dome with similar radius (top, purple) in the region of the in-plane E^1_{2g} and out-of-plane A_{1g} modes. A sketch of the two vibrational modes is displayed as inset. The gray dashed lines highlight the position of the peaks originating from the bulk flake, while the peaks at lower energy with respect to the bulk modes originate from the domes. The purple lines are set in correspondence of the modes of the random dome, to highlight the redshift of the modes of the patterned dome. d) Red-shifts for the in-plane mode (see sketch as inset) with respect to an unstrained ML measured on top of several random (purple) and patterned (green, $S = 3$ μm) domes with analogous dimensions, plotted as a function of the estimated in-plane strain. The gray line is a linear fit to the data, leading to the Grüneisen parameter $\gamma_{E^1_{2g}}$ reported as inset.

perfectly isotropic strains, creating the conditions for long-lived excitons[13] promising for Bose condensates,[42] or for engendering pseudo-magnetic fields[28,43,44] that could be potentially exploited for the generation of quasi-persistent currents.[29] Furthermore, the method proposed in this work is relevant for applications in photovoltaics, photocatalysis, and photodetection,[18] allowing to create the conditions for broadband absorption and harvesting of the photoexcited charge carriers by funneling.[13] Finally, strains as high as 10% have been predicted to activate and make TMDs potentially efficient as electrochemical hydrogen catalysts.[21,30,31]

The technique presented in this communication is highly versatile, and might be exploited in diverse systems—possibly including other TMDs,[26] h-BN,[27] graphene,[45] and other layered materials[46]—allowing the strain engineering of a wider class of 2D materials.

Experimental Section

EBL Patterning: The fabrication of H-opaque masks was performed by means of EBL employing a Vistec EPBG 5HR system working at 100 kV. A HSQ negative-tone e-beam resist was employed because of its property to be H-opaque under the irradiation conditions used in this work. Ordered arrays of octagonal openings with the desired diameter were patterned on a HSQ masking layer deposited on top of the sample surface. The thickness of the resist layer was controlled by varying the resist concentration and spinning speed. An electron dose of 150 μC cm^{-2} and an aqueous development solution of tetramethyl ammonium hydroxide at 2.4% were used for the patterning of the HSQ masks.

AFM Measurements: AFM measurements were performed with two different instruments and by using different tips. The data were then analyzed by different co-authors and led to analogous results. In particular, AFM measurements were performed by using:

–A Veeco Digital Instruments Dimension D3100 microscope equipped with a Nanoscope IIIa controller, employing Tapping Mode monolithic

silicon probes with a nominal tip curvature radius of 5–10 nm and a force constant of 40 N m^{-1};
–A Nanowizard III from JPK, equipped with Vortex controller, employing Tapping Mode silicon probes with a measured tip curvature radius of 50+/–10 nm and a force constant of 40 N m^{-1}.

The convolution of the tip used during the measurements was duly taken into account. All the data were taken at room temperature and under the same ambient conditions (atmospheric pressure). All the data were analyzed with the Gwyddion software.

Optical Measurements: For second harmonic generation measurements, a supercontinuum laser tuned at ≈900 nm with a ≈50 ps pulse width and a 77.8 MHz repetition rate was used. The second harmonic signal was collected by means of a 750 mm focal length monochromator ACTON SP750 equipped with a 1200 groove mm^{-1} grating and detected by a back-illuminated Si CCD Camera (model 100BRX) by Princeton Instruments. A 100 × objective with NA = 0.9 was employed to excite and collect the light.

For Raman measurements, the excitation laser was provided by a single frequency Nd:YVO4 lasers (DPSS series by Lasos) with emission wavelength equal to 532.2 nm. The Raman signal was spectrally analyzed with the same monochromator and CCD described above. The micro-Raman (μ-Raman) spectral resolution was 0.7 cm^{-1}. The laser light was filtered out by a very sharp high-pass Razor edge filter at 535 nm (Semrock). The same objective described above was used for laser excitation/collection. The laser spot size was experimentally determined as follows: The laser was scanned across a reference sample, lithographically patterned with features of known width (1 μm). The intensity of the reflected light was fitted with the ideal reflectance profile, convolved with a Gaussian peak. The standard deviation of this peak, obtained as a fitting parameter, provided an estimate of $\sigma = 0.23 \pm 0.01$ μm.

For micro-photoluminescence (μ-PL) measurements, the excitation laser was provided by a diode laser at 405 nm. Due to the poor efficiency of the emitted signal, the PL emission was spectrally analyzed by means of a 200 mm focal length monochromator Isoplane160 equipped with a 150 groove mm^{-1} grating and detected by a back-illuminated Si CCD Camera (model 100BRX) by Princeton Instruments. The same objective described above was used for excitation/collection.

Supporting Information

Supporting Information is available from the Wiley Online Library or from the author.

Acknowledgements

The authors acknowledge the support by Sapienza Università di Roma under the grants "Ricerche Ateneo" 2018 and 2019 (A.P. and M.F.). M.F. and G.P. acknowledge support and funding from the Italian Ministry for Education, University and Research within the Futuro in Ricerca (FIRB) program (project DeLIGHTeD, Prot. RBFR12RS1W). E.B., A.P., and M.F. acknowledge funding from the Regione Lazio programme "Progetti di Gruppi di ricerca" legge Regionale n. 13/2008 (SINFONIA project, prot. n. 85-2017-15200) via LazioInnova spa. The authors acknowledge fund support from Australian Research Council (ARC) (numbers DE140100805 and DP180103238), and ARC Centre of Excellence in Future Low-Energy Electronics Technologies (project number CE170100039).

Conflict of Interest

The authors declare no conflict of interest.

Keywords

2D materials, bubbles, engineering, MoS_2 monolayers, nonuniform strains

Received: April 7, 2020
Revised: May 21, 2020
Published online:

[1] C. Lee, X. Wei, J. W. Kysar, J. Hone, *Science* **2008**, *321*, 385.
[2] S. Bertolazzi, J. Brivio, A. Kis, *ACS Nano* **2011**, *5*, 9703.
[3] S. Deng, A. V. Sumant, V. Berry, *Nano Today* **2018**, *22*, 14.
[4] L. Zhang, A. Zunger, *Nano Lett.* **2015**, *15*, 949.
[5] H. Yuan, Z. Liu, G. Xu, B. Zhou, S. Wu, D. Dumcenco, K. Yan, Y. Zhang, S.-K. Mo, P. Dudin, V. Kandyba, M. Yablonskikh, A. Barinov, Z. Shen, S. Zhang, Y. Huang, X. Xu, Z. Hussain, H. Y. Hwang, Y. Cui, Y. Chen, *Nano Lett.* **2016**, *16*, 4738.
[6] D. J. Trainer, A. V. Putilov, C. Di Giorgio, T. Saari, B. Wang, M. Wolak, R. U. Chandrasena, C. Lane, T.-R. Chang, H.-T. Jeng, H. Lin, F. Kronast, A. X. Gray, X. Xi, J. Nieminen, A. Bansil, M. Iavarone, *Sci. Rep.* **2017**, *7*, 40559.
[7] D. Xiao, G.-B. Liu, W. Feng, X. Xu, W. Yao, *Phys. Rev. Lett.* **2012**, *108*, 196802.
[8] P. Johari, V. B. Shenoy, *ACS Nano* **2012**, *6*, 5449.
[9] C.-H. Chang, X. Fan, S.-H. Lin, J.-L. Kuo, *Phys. Rev. B* **2013**, *88*, 195420.
[10] D. Lloyd, X. Liu, J. W. Christopher, L. Cantley, A. Wadehra, B. L. Kim, B. B. Goldberg, A. K. Swan, J. S. Bunch, *Nano Lett.* **2016**, *16*, 5836.
[11] H. J. Conley, B. Wang, J. I. Ziegler, R. F. Haglund Jr., S. T. Pantelides, K. I. Bolotin, *Nano Lett.* **2013**, *13*, 3626.
[12] D. J. Trainer, Y. Zhang, F. Bobba, X. Xi, S.-W. Hla, M. Iavarone, *ACS Nano* **2019**, *13*, 8284.
[13] E. Blundo, M. Felici, T. Yildirim, G. Pettinari, D. Tedeschi, A. Miriametro, B. Liu, W. Ma, Y. Lu, A. Polimeni, *Phys. Rev. Res.* **2020**, *2*, 012024(R).
[14] J. Chaste, A. Missaoui, S. Huang, H. Henck, Z. Ben Aziza, L. Ferlazzo, C. Naylor, A. Balan, A. T. C. Johnson Jr., R. Braive, A. Ouerghi, *ACS Nano* **2018**, *12*, 3235.
[15] J. Pető, G. Dobrik, G. Kukucska, P. Vancsó, A. A. Koós, J. Koltai, P. Nemes-Incze, C. Hwang, L. Tapasztó, *npj 2D Mater. Appl.* **2019**, *3*, 39.
[16] C. Ma, J. Yan, Y. Huang, Z. Zheng, G. Yang, *Nanotechnology* **2020**, *31*, 065204.
[17] M. Ghorbani-Asl, S. Borini, A. Kuc, T. Heine, *Phys. Rev. B* **2013**, *87*, 235434.
[18] J. Feng, X. Qian, C.-W. Huang, J. Li, *Nat. Photonics* **2012**, *6*, 866.
[19] R. Schmidt, I. Niehues, R. Schneider, M. Drüppel, T. Deilmann, M. Rohlfing, S. M. de Vasconcellos, A. Castellanos-Gomez, R. Bratschitsch, *2D Mater.* **2016**, *3*, 021011.
[20] J. Chaste, A. Missaoui, S. Huang, H. Henck, Z. Ben Aziza, L. Ferlazzo, C. Naylor, A. Balan, A. T. C. Johnson Jr., R. Braive, A. Ouerghi, *ACS Nano* **2018**, *12*, 3235.
[21] H. Li, C. Tsai, A. L. Koh, L. Cai, A. W. Contryman, A. H. Fragapane, J. Zhao, H. S. Han, H. C. Manoharan, F. Abild-Pedersen, J. K. Nørskov, X. Zheng, *Nat. Mater.* **2016**, *15*, 48.
[22] S. Xie, L. Tu, Y. Han, L. Huang, K. Kang, K. U. Lao, P. Poddar, C. Park, D. A. Muller, R. A. DiStasio Jr., J. Park, *Science* **2018**, *359*, 1131.
[23] C. Martella, C. Mennucci, A. Lamperti, E. Cappelluti, F. Buatier de Mongeot, A. Molle, *Adv. Mater.* **2018**, *30*, 1705615.
[24] D. Lloyd, X. Liu, N. Boddeti, L. Cantley, R. Long, M. L. Dunn, J. S. Bunch, *Nano Lett.* **2017**, *17*, 5329.
[25] E. Khestanova, F. Guinea, L. Fumagalli, A. Geim, I. Grigorieva, *Nat. Commun.* **2016**, *7*, 12587.

[26] D. Tedeschi, E. Blundo, M. Felici, G. Pettinari, B. Liu, T. Yildrim, E. Petroni, C. Zhang, Y. Zhu, S. Sennato, Y. Lu, A. Polimeni, *Adv. Mater.* **2019**, *31*, 1903795.
[27] L. He, H. Wang, L. Chen, X. Wang, H. Xie, C. Jiang, C. Li, K. Elibol, J. Meyer, K. Watanabe, T. Taniguchi, Z. Wu, W. Wang, Z. Ni, X. Miao, C. Zhang, D. Zhang, H. Wang, X. Xie, *Nat. Commun.* **2019**, *10*, 2815.
[28] H. Ochoa, R. Zarzuela, Y. Tserkovnyak, *Phys. Rev. Lett.* **2017**, *118*, 026801.
[29] M. Taillefumier, V. K. Dugaev, B. Canals, C. Lacroix, P. Bruno, *Phys. Rev. B* **2008**, *78*, 155330.
[30] D. Voiry, J. Yang, M. Chhowalla, *Adv. Mater.* **2016**, *28*, 6197.
[31] X. Chen, G. Wang, *Phys. Chem. Chem. Phys.* **2016**, *18*, 9388.
[32] T. F. Aslyamov, E. S. Iakovlev, I. S. Akhatov, P. A. Zhilyaev, *J. Chem. Phys.* **2020**, *152*, 054705.
[33] E. S. Iakovlev, P. A. Zhilyaev, I. S. Akhatov, *J. Phys.: Conf. Ser.* **2019**, *1147*, 012006.
[34] K. Yue, W. Gao, R. Huang, K. M. Liechti, *J. Appl. Phys.* **2012**, *112*, 083512.
[35] N. Kumar, S. Najmaei, Q. Cui, F. Ceballos, P. M. Ajayan, J. Lou, H. Zhao, *Phys. Rev. B* **2013**, *87*, 161403(R).
[36] Y. Li, Y. Rao, K. F. Mak, Y. You, S. Wang, C. R. Dean, T. F. Heinz, *Nano Lett.* **2013**, *13*, 3329.
[37] P. Wang, W. Gao, Z. Cao, K. M. Liechti, R. Huang, *J. Appl. Mech.* **2013**, *80*, 040906.
[38] W. B. Fichter, *NASA Tech. Pap.* **1997**, *3658*, 1.
[39] Y. Wang, C. Cong, C. Qiu, T. Yu, *Small* **2013**, *9*, 2857.
[40] C. Rice, R. J. Young, R. Zan, U. Bangert, D. Wolverson, T. Georgiou, R. Jalil, K. S. Novoselov, *Phys. Rev. B* **2013**, *87*, 081307(R).
[41] T. M. G. Mohiuddin, A. Lombardo, R. R. Nair, A. Bonetti, G. Savini, R. Jalil, N. Bonini, D. M. Basko, C. Galiotis, N. Marzari, K. S. Novoselov, A. K. Geim, A. C. Ferrari, *Phys. Rev. B* **2009**, *79*, 205433.
[42] J. J. Esteve-Paredes, S. Pakdel, J. J. Palacios, *Phys. Rev. Lett.* **2019**, *123*, 077402.
[43] F. Guinea, M. I. Katsnelson, A. K. Geim, *Nat. Phys.* **2010**, *6*, 30.
[44] M. Cazalilla, H. Ochoa, F. Guinea, *Phys. Rev. Lett.* **2014**, *113*, 077201.
[45] E. Stolyarova, D. Stolyarov, K. Bolotin, S. Ryu, L. Liu, K. T. Rim, M. Klima, M. Hybertsen, I. Pogorelsky, I. Pavlishin, K. Kusche, J. Hone, P. Kim, H. L. Stormer, V. Yakimenko, G. Flynn, *Nano Lett.* **2009**, *9*, 332.
[46] J. Felton, E. Blundo, S. Ling, J. Glover, Z. R. Kudrynskyi, O. Makarovsky, Z. D. Kovalyuk, E. Besley, G. Walker, A. Polimeni, A. Patané, *Molecules* **2020**, *25*, 2526.

